Atomistic mechanisms of the initial oxidation of stepped Cu₃Au(100)

Yaguang Zhu,[1] Dongxiang Wu,[1] Chaoran Li,[1] Xiao Tong,[2] J. Anibal Boscoboinik,[2]
Jerzy T. Sadowski,[2] and Guangwen Zhou[1,*]

[1]*Department of Mechanical Engineering & Materials Science and Engineering Program,*
State University of New York, Binghamton, New York 13902, USA
[2]*Center for Functional Nanomaterials, Brookhaven National Laboratory, Upton, New York 11973, USA*

Alloy oxidation is complex and involves several critical processes that lack understanding on the atomic level. Here, we report an atomistic picture of the initial-stage oxidation of stepped Cu₃Au(100) using a combination of surface science tools and modeling to illuminate the microscopic processes underlying oxygen-adsorption-induced structural and compositional changes. Pristine Cu₃Au(100) consists of wide CuAu-terminated terraces and narrow Cu-terminated terraces separated by monatomic steps. Counterintuitive to the common expectations of the adsorbate-induced surface segregation of the more reactive alloy component, our observations demonstrate that the oxygen adsorption leads to the exfoliation of the outermost CuAu layer, thereby exposing the inner Cu plane to O attack. This occurs via the oxygen-assisted abstraction of Au and Cu atoms from step edges and CuAu terraces, which generates many Cu adatoms aggregating into Cu clusters and Au adatoms dissolving into the bulk. The oxygen adsorption onto fourfold hollow sites of the exposed Cu plane results in nucleation and growth of the $c(2 \times 2)$-O superstructure, which can be fit well by the Johnson-Mehl-Avrami-Kolmogorov theory with a site-saturated nucleation mechanism.

I. INTRODUCTION

Oxidation is a degradation phenomenon of a metallic material resulting from chemical reactions in which the metal combines with oxygen to form oxides. It is ubiquitous because most metals are reactive in their functioning environments and have a strong driving force to transform to their low-energy oxide state. Alloying is often used to modify material properties with respect to pure metals. One classic example of alloying is the development of alloys with enhanced oxidation resistance resulting from the formation of a stable and protective oxide layer. Despite its seeming simplicity, oxidation is a rather complicated process because it covers many fields of materials science, ranging from basic thermodynamics of gas-surface reactions, defect chemistry, surface/interface, bulk and short-circuit diffusion, and phase transformations to interface-reaction-induced stress generation and relaxation, many of which are coupled and involved from the onset of the reaction. Much of our current knowledge of oxidation is derived from the work based on the growth of macroscopically thick oxide that is too coarse to reflect the microscopic details of the early-stage oxidation. Microscopic atomic-scale observations of alloy oxidation are still rare but are essential for developing a fundamental understanding of the environmental stability and functionality of alloys. Compared with the oxidation of pure metals, alloy oxidation is generally much more complex. The possible effects of alloying on the oxidation process include different oxygen affinities of the alloying elements, formation

of multiple oxides and solid solubility between them, and different mobilities of various metal ions in the alloy and the oxides. A detailed understanding of the key processes taking place in the critical early stages of the oxidation is even more challenging because of the overwhelming presence of structural defects at the surface and the difficulty of atomically probing the complex interplay among oxygen atoms, alloying elements, and structural defects.

Herein, we address the early-stage oxidation of Cu₃Au(100) with the use of a combination of scanning tunneling microscopy (STM) imaging, low-energy electron diffraction (LEED), low-energy ion scattering (LEIS), and synchrotron-based ambient-pressure x-ray photoelectron spectroscopy (AP-XPS) to provide complementary information on surface structure, composition, and chemistry in conjunction with atomistic modeling. The Cu₃Au(100) surface examined in this paper consists of a series of monatomic atomic steps alternating with flat terraces, a characteristic morphology common to most crystal surfaces. We seek the effects of alloying and atomic steps on oxygen-adsorption-induced compositional and structural transformation at the alloy surface. The Cu-Au system is considered for both its fundamental and practical importance. Fundamentally, the dramatic difference in the oxygen affinity between Cu and Au atoms allows some of the features of the early-stage alloy oxidation to be examined without the complication of competing oxygen adsorption by reactive alloying elements. Practically, bimetallic Cu-Au alloys show improved reactivity over the single metal counterparts [1] for various catalytic oxidation reactions including CO oxidation [2,3], CO₂ reduction [4,5], methanol production

*gzhou@binghamton.edu

[6,7], and the water-gas shift reaction [8,9]. These catalytic reactions are initiated from the adsorption and dissociation of oxygen-containing species, which depend on surface structure, composition, and coordination environment around defective sites. A proper interpretation of the catalytic properties of Cu-Au alloys requires a precise knowledge of the surface composition and structural transformation induced by oxygen adsorption. A Cu_3Au surface can be a model system for establishing the fundamental principles to control the adsorption properties of alloys by tuning the segregation and desegregation of the alloying elements with the chemical stimuli.

II. EXPERIMENTAL AND COMPUTATIONAL DETAILS

A $Cu_3Au(100)$ single crystal (Princeton Scientific Corp.) was used for the oxidation experiments. The $Cu_3Au(100)$ was cut to within $0.1°$ to the (100) crystallographic orientation and polished to a mirror finish. A clean surface can be achieved by repeated cycles of Ar+ sputtering at room temperature (2×10^{-5} Torr of Ar^+, $8 \mu A \, cm^{-2}$, 1.5 keV) and ultrahigh vacuum (UHV) annealing at $600 °C$ for 10 min. The STM experiments were performed with an UHV system consisting of a sample preparation chamber (base pressure $\sim 1 \times 10^{-10}$ Torr) for the surface preparation and an STM chamber (base pressure $\sim 1 \times 10^{-11}$ Torr) for surface imaging. Surface cleanliness and order were checked by STM, LEED, and XPS. Oxidation was performed by exposing the clean surface to high-purity (99.9999%) oxygen gas at an oxygen partial pressure (pO_2) of 1×10^{-6} Torr and $350 °C$. The STM imaging was performed at room temperature with an electrochemically etched tungsten tip, and the bias was applied on the sample. Separate UHV systems equipped with LEED and LEIS with a SPECS Phoibos 100 energy analyzer were used to further confirm the crystal structure and surface composition of the $Cu_3Au(100)$ prepared using a similar procedure as that in the STM measurements.

AP-XPS was employed to monitor the surface composition and chemistry evolution of the $Cu_3Au(100)$ as a function of the O_2 exposure at $pO_2 = 1 \times 10^{-6}$ Torr and $350 °C$. The AP-XPS experiments were performed at the IOS beamline of the National Synchrotron Light Source II (NSLS-II), Brookhaven National Laboratory. The detailed instrument setup can be found from previous work [10–13]. In short, the multiple differential pumping stages between the main chamber and the hemispherical analyzer allow for eliminating the scattering effect of gas molecules and continuously acquiring XPS spectra in the presence of gas at the pressure of 1×10^{-6} Torr. The photon energy range of the beamline is from 250 to 2000 eV, which covers O $1s$, Cu $2p$, Cu $3p$, and Au $4f$ core levels and Cu LMM relevant for this paper. Real-time monitoring of the surface composition evolution induced by surface segregation was performed by acquiring spectra of the Au $4f$ core level *in situ*. All spectra were collected at a takeoff angle of $20°$ between the sample surface and the electron analyzer optics of the XPS spectrometer. Binding energies in each spectrum were referred to the Fermi level for correction, and XPS spectra were analyzed with the Voigt line shape and Shirley-type background. Line shape of

a Gaussian/Lorentzian sum formula modified using an exponential tail function was introduced for accurate peak fitting and deconvolution. Full width at half maximum (FWHM) of Au was 0.5–0.6 eV for alloy Au and 0.4–0.5 eV for metallic Au. Integrated peak areas of each Au species were used to calculate the relative composition evolution.

The density functional theory (DFT) calculations made use of the Vienna *Ab initio* Simulation Package, employing plane-wave functionals with the projector augmented wave approach [14–17]. The generalized gradient approximation with the Perdew-Burke-Ernzerhof exchange-correlation functional was used to evaluate the exchange-correlation energy [18,19]. Our computational framework is like previous work [20]. The plane wave energy cutoff energy was set as 400 eV. Monkhorst-Pack k-point grids of $4 \times 4 \times 1$ and $4 \times 2 \times 1$ were used for the CuAu surface calculations [21]. We used period slabs with a vacuum spacing of 12 Å to model the surface, and the slab is composed of five layers with the bottom two layers fixed. All the structures were fully relaxed until the force acting on each atom was $<0.015 eV/Å$. The $Cu_3Au(100)$ surface is known to ripple with the Au atoms being displaced above the Cu atoms. The magnitude of the rippling found experimentally (~ 0.12 Å [22], ~ 0.04 Å [23]) and theoretically (~ 0.18 Å [24], ~ 0.15 Å [25]) is reasonably reproduced in our DFT calculations (~ 0.26 Å). Our DFT calculations of the O adsorption at $Cu_3Au(100)$ are based on the fully relaxed $Cu_3Au(100)$, for which the surface ripping effect is incorporated.

We investigated the vacancy formation energy of Cu and Au in our DFT modeling to explore the surface structure evolution. The most stable configuration identified after removing a Cu or Au atom was used as a starting configuration for the next atom removal. The vacancy formation energy was computed using the equation

$$E_{vac} = E_{slab}^{tot} - E_{ref} - E_{atom}, \quad (1)$$

where E_{slab}^{tot} is the total energy of the whole CuAu system, E_{ref} is the free energy of the slab with one Cu or Au vacancy, and E_{atom} is the free energy of single Cu/Au atom in the bulk structure. All the atomic structures were visualized using the Visualization for Electronic and Structure Analysis.

III. RESULTS

A. STM imaging

Cu_3Au has a cubic $L1_2$-ordered structure and transforms to a substitutionally disordered face-centered cubic (fcc) lattice on heating over the bulk order-disorder transition temperature of $\sim 390 °C$. In $L1_2$-ordered Cu_3Au, Au atoms occupy the corners of the fcc unit cell and Cu the face centers [Fig. 1(a)]. Therefore, the ordered $Cu_3Au(100)$ surface could be terminated in a plane of (i) pure Cu (i.e., CuCu plane) or (ii) in a plane consisting of equal numbers of Cu and Au atoms (CuAu plane) [26]. Figure 1(b) shows a LEED pattern of the $Cu_3Au(100)$ crystal that was annealed at $350 °C$ in UHV to restore the chemical order of the alloy. The LEED pattern reveals a $p(1 \times 1)$ symmetry and a clear $c(2 \times 2)$ superstructure, as marked in Fig. 1(b). The $c(2 \times 2)$ superstructure is due to the $L1_2$-ordered lattice and suggests the CuAu surface
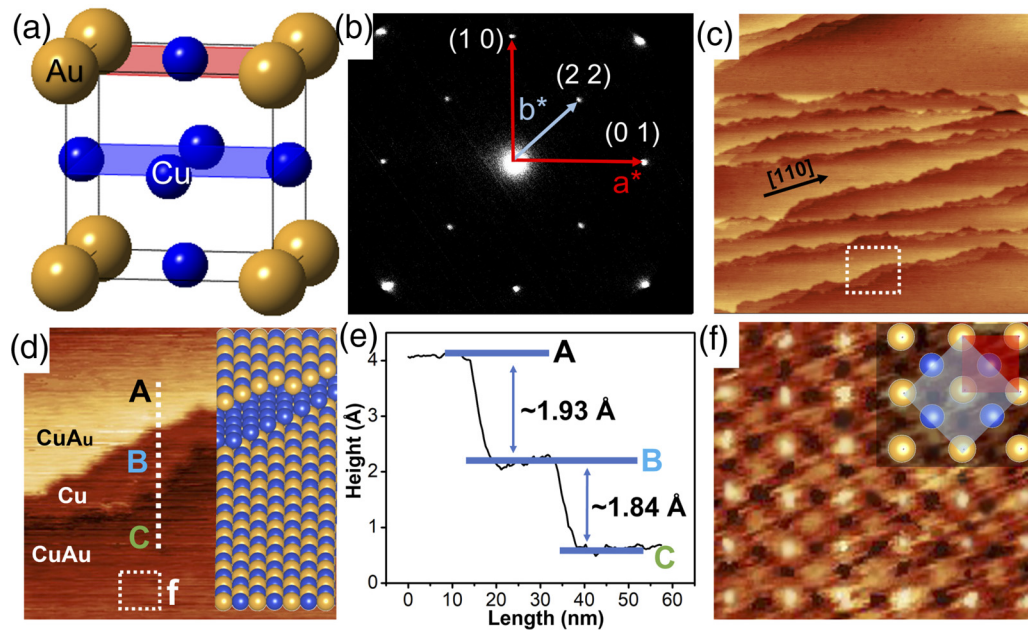
FIG. 1. (a) The crystal model of L1$_2$ ordered Cu$_3$Au. The possible surface terminations in a plane CuAu or pure Cu are marked in purple and blue, respectively. (b) Low-energy electron diffraction (LEED) pattern of clean ordered Cu$_3$Au(100), where the (2,2) spot corresponds to the superlattice cell shown in the inset of (f). Primary electron energy: $E = 25$ eV. (c) Topographic scanning tunneling microscopy (STM) image (size: 500×500 nm^2) of an ordered Cu$_3$Au(100) surface, showing that the surface consists of wide and narrow terraces with a preferred terrace edge orientation along [011]. (d) Zoomed-in STM image of the stepped region as marked by the white dashed box in (c) (size: 40×40 nm^2). The inset shows schematically the surface termination of the wide and narrow terraces, gold and blue balls represent Au and Cu atoms, respectively. (e) Surface profile along the white dashed line marked in (d), indicating that the terraces are separated by monolayer atomic steps. (f) Atomically resolved STM image of the wide terrace as marked by the white dashed square in (d) (size: 2×2 nm^2). The upper-right inset shows schematically the $c(2 \times 2)$ superstructure of the ordered Cu$_3$Au(100). The tunneling conditions for the STM imaging: (c) $V_B = 2$ V, $I_T = 0.1$ nA, (d) and (f) $V_B = 0.1$ V, $I_T = 1$ nA.

termination. Figure 1(c) displays a representative STM topographic image of the Cu$_3$Au(100) surface, showing that the well-annealed surface consists of alternating wide and narrow terraces separated by atomic steps that exhibit a sawtoothlike, zigzag appearance with the preferred terrace edge orientation along the [110] direction. Figure 1(d) presents a zoomed-in STM image of the stepped region, as marked by the white dashed box in Fig. 1(c), showing that the atomic steps consist of a wide terrace ($\geqslant$50 nm) and a narrow terrace ($\sim$5–10 nm). As illustrated schematically in the inset of Fig. 1(d) and confirmed later by the step height profile and atomically resolved STM imaging analysis, the wide terraces are terminated by the CuAu plane, whereas the narrow terraces have the surface termination of the pure Cu plane. Figure 1(e) displays the STM height profile along the white dashed line in Fig. 1(d), showing a step height of $\sim$1.93 Å between the upper CuAu(100)-terminated terrace (A) and the lower Cu(100)-terminated terrace (B) but a slightly smaller step height of $\sim$1.84 Å between the Cu(100)-terminated terrace (B) and the bottom CuAu(100)-terminated terrace (C). The slight differences in the step heights can be attributed to the upward relaxation of Au atoms in the CuAu-terminated surface of L1$_2$-ordered Cu$_3$Au(100) [24]. Since the L1$_2$-ordered Cu$_3$Au has a lattice constant of $\sim$3.75 Å [27,28], the measured step heights correspond to monoatomic steps. The surface terraces separated by monoatomic steps should have different chemical configurations, i.e., the surface planes of CuAu and pure Cu, as highlighted in the inset of Fig. 1(d).

Figure 1(f) shows an atomically resolved STM image from the wide terrace, as marked by the white dashed box in Fig. 1(d). Although it is challenging to chemically resolve Cu and Au atoms by STM imaging, one can find that the surface consists of two types of atoms, where the bright intensity ones have a larger surface height (by $\sim$0.13 Å) than the weak intensity ones and correspond to Au, whereas the weak intensity ones can be assigned as Cu. It is worth mentioning that STM is sensitive to topography convoluted with the electronic density of states, but the good match of the surface height difference between the Au and Cu atoms measured here with other experimental tools (0.12 Å by ion scattering spectroscopy (ISS) [22]) and modeling results ($\sim$0.18 Å [24], $\sim$0.15 Å [25]) suggests that the STM image contrast in Fig. 1(f) is dominated by geometric rather than electronic effects. The measured distance between adjacent bright (Au) atoms is $\sim$3.7 Å, which is also consistent with the lattice constant of the Cu$_3$Au unit cell. The upper-right inset in Fig. 1(f) shows schematically the arrangement of Au and Cu atoms in the CuAu-terminated surface, in which the marked parameters of the $p(1 \times 1)$ and $c(2 \times 2)$ unit cells are related by $b = \sqrt{2}a$ with the 45° rotation angle of the two cells. This makes the Wood's notation of the surface structure of the $c(2 \times 2)$. Therefore, it can be determined that the wide terraces are terminated by the CuAu plane of the L1$_2$-ordered Cu$_3$Au(100).

The above LEED and STM imaging demonstrate that the pristine surface prepared from the UHV annealing consists of alternating wide and narrow terraces separated by
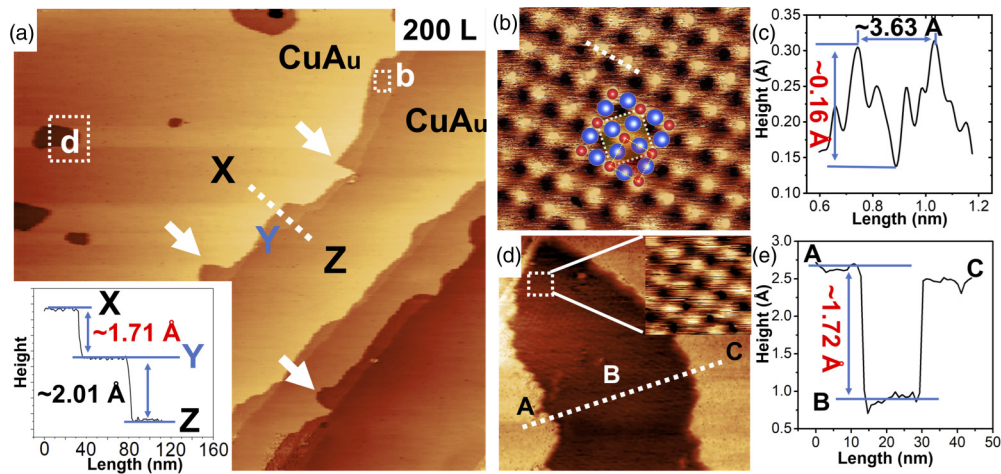
FIG. 2. (a) Representative scanning tunneling microscopy (STM) image (size: 300×300 nm^2) of the Cu$_3$Au(100) obtained after 200 L of O$_2$ exposure at 350 °C. The lower-left inset is the surface profile along the white dashed line across the CuAu terraces (X, Z) and the narrow, Cu-terminated terrace (Y). (b) High-resolution STM image (size: 2×2 nm^2) of the narrow terrace marked by white dashed box b in (a), in which only O atoms are visible. The $c(2 \times 2)$-O structure model is overlaid onto the STM image (the blue and red balls represent Cu and O atoms, respectively). (c) Surface profile along the white dashed line across two adjacent O atoms in (b). (d) Zoomed-in STM image (size: 20×20 nm^2) of the monolayer depression within the wide terrace marked with dashed box d in (a). The upper-right inset is an atomically resolved STM image (size: 2×2 nm^2) of the depression bottom marked with the dashed box. (e) Surface profile along the white dashed line across the terrace depression in (d). The tunneling conditions for STM imaging: (a) $V_B = 2$ V, $I_T = 0.1$ nA, (b) $V_B = 0.05$ V, $I_T = 1$ nA, and (d) $V_B = 1.0$ V, $I_T = 0.1$ nA.

monoatomic steps, and the wide terraces have the surface termination of the CuAu plane, whereas the narrow terraces have the surface termination of the pure Cu plane. This provides the baseline to understand the onset of the surface oxidation and the resultant surface composition and structure evolution during the O$_2$ annealing. Figure 2(a) shows a representative large-scale STM image of the Cu$_3$Au(100) surface after 200 Langmuir (L) of O$_2$ exposure at 350 °C. The surface is still composed of wide (CuAu-terminated) and narrow (Cu-terminated) terraces, but the average extension of the narrow terraces is now of the order of ∼15 nm, which is about a factor of 2 wider than that of the pristine surface [Fig. 1(c)]. The widening of the narrow terraces is caused by the oxygen attack along the step edge of the wide terraces, which results in the receding motion of the step edges and the formation of local recessions into the wide terraces, as indicated by the white arrows in Fig. 2(a). As a result, the step edges become less zigzag with relatively long straight segments because the protruding portion of the step edges is etched away first. In addition, the oxygen attack also takes place within the wide (CuAu) terraces, which results in the extraction of Au and Cu atoms from the topmost surface layer and leads to the formation of depressions (pits) in the terraces, as marked by white dashed box d in Fig. 2(a). The lower-left inset in Fig. 2(a) displays the STM height profile taken along the white dashed line across terraces X, Y, and Z. Areas X and Z correspond to the wide, CuAu-terminated terraces that are separated by the narrow, Cu-terminated terrace (terrace Y). The line profile shows a step height of ∼1.71 Å between terraces X and Y, which is ∼0.2 Å smaller than the step height (∼1.9 Å) for the pristine surface [Figs. 1(d) and 1(e)]. By contrast, the step height between terraces Y and Z is ∼2.0 Å, a slight increase (by 0.2 Å) from the corresponding step height of the pristine surface [Figs. 1(d) and 1(e)].

Figure 2(b) shows a zoomed-in STM image obtained from the Cu-terminated, narrow terrace, as marked by white dashed box b in Fig. 2(a). The atomically resolved STM image reveals a $c(2 \times 2)$ structure of adsorbed oxygen, in which the oxygen atoms occupy the fourfold hollow sites of the Cu-terminated (100) terrace with 0.5 monolayer (ML) oxygen coverage, as shown schematically by the overlaid atomic structure in Fig. 2(b). The $c(2 \times 2)$-O structure has been widely observed from oxygen adsorption on Cu(100) [14,29,30]. The $c(2 \times 2)$-O formation observed here indicates that the Cu-terminated terraces of the L1$_2$-ordered Cu$_3$Au(100) have similar behavior in the oxygen adsorption on Cu(100). Figure 2(c) displays the height profile along the white dashed line in Fig. 2(b), showing a lateral distance of 3.6 Å between the bright spots and a surface corrugation of ∼0.2 Å. The measured distance equals the distance between adjacent O atoms in $c(2 \times 2)$-O, which indicates that the bright spots correspond to O atoms, and the Cu atoms locating at the bridge sites of O atoms remain invisible in the STM image. This is also consistent with DFT calculations showing that the local density of states of O are higher than that of Cu in $c(2 \times 2)$-O [31]. By comparison with the step heights for the pristine surface [Figs. 1(d) and 1(e)], the O adsorption by the Cu-terminated terrace and the resultant upward relaxation of the surface O atoms give rise to the decreased step height (∼1.71 Å) between the lower Cu-terminated terrace and the upper CuAu-terminated terrace but an increased step height (∼2.01 Å) between the lower CuAu-terminated terrace and the upper Cu-terminated terrace [the inset in Fig. 2(a)].

Figure 2(d) shows a zoomed-in STM image obtained from the depression within the wide terrace, as marked by white dashed box d in Fig. 2(a). The topographic STM image reveals that the bottom surface of the depression displays the square-gridlike structure, which is evident in the inset zoomed-in
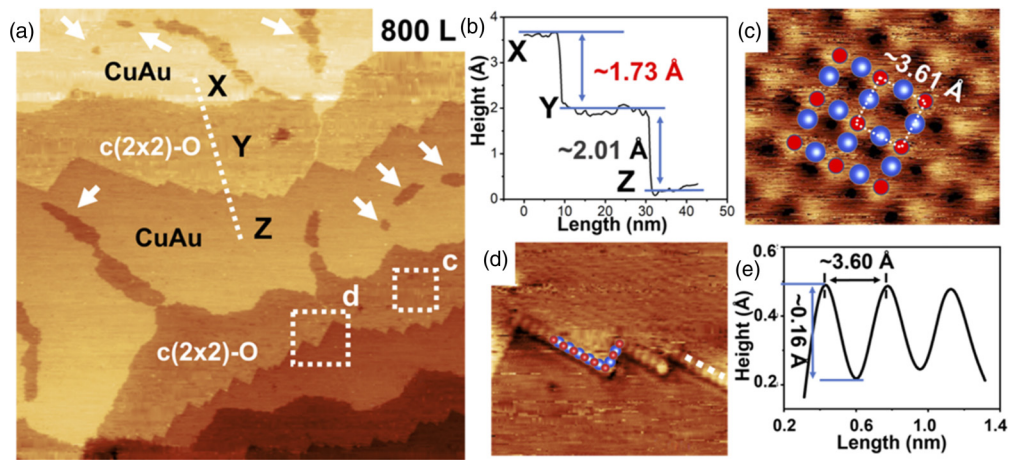
FIG. 3. (a) Scanning tunneling microscopy (STM) image (size: $300 \times 300 \, \text{nm}^2$) of the Cu$_3$Au(100) surface after 800 L of O$_2$ exposure at 350 °C. (b) STM line profile along the white dashed line across the CuAu terrace (Y) and the adjacent oxygenated Cu terraces (X, Z) in (a). (c) Atomically zoomed-in STM image (size: $2 \times 2 \, \text{nm}^2$) of the oxygenated Cu terrace marked with white dashed box c in (a), inset is the $c(2 \times 2)$-O structure overlaid on the STM image. (d) Zoomed-in STM image (size: $40 \times 40 \, \text{nm}^2$) of the stepped region marked with white dashed box d in (a), overlaid onto the STM image is the adsorption of O atoms onto the fourfold hollow sites made by the Cu atoms at the step edge. The blue and red balls represent Cu and O atoms, respectively. (e) STM line profile along the white dashed line along the step edge of the $c(2 \times 2)$-O terrace in (d). The tunneling conditions for STM imaging: (a) $V_B = 2 \, \text{V}$, $I_T = 0.1 \, \text{nA}$, (c) and (d) $V_B = 0.35 \, \text{V}$, $I_T = 1 \, \text{nA}$.

STM image showing the same $c(2 \times 2)$-O structure as that in Fig. 2(b). This suggests that it is a ML depression, and the bottom surface of the depression is terminated by the Cu plane with adsorbed O at the fourfold hollow sites of Cu atoms. The ML depression is further confirmed by the STM height profile taken along the white dashed line across the depression in Fig. 2(d). As shown in Fig. 2(e), the depression has a depth of $\sim$1.72 Å, which matches well with the height of the monoatomic step between the lower oxygenated Cu terrace and the upper CuAu terrace, as shown in the inset of Fig. 2(a).

The above STM observations indicate that the O$_2$ exposure results in O adsorption at the fourfold hollow sites of the Cu-terminated terraces. Meanwhile, the oxygen attack also leads to the decomposition of the topmost layer of the wide, CuAu-terminated terraces via the formation of ML depressions and step-edge decay. To further confirm this trend, the evolution of the surface morphology and structure was monitored as a function of the O$_2$ exposure at 350 °C and pO$_2 = 1 \times 10^{-6}$ Torr. Figure 3(a) illustrates an STM image of the surface morphology after 800 L of O$_2$ exposure. The surface still consists of wide (CuAu-terminated) and narrow (Cu-terminated) terraces separated by monoatomic steps, as confirmed by the surface profile shown in Fig. 3(b). The average extension of the Cu terraces is of the order of $\sim$30 nm, about a factor of 3 larger than that of the pristine surface [Fig. 1(c)]. The widening of the Cu terraces is caused by the step-edge decay of the CuAu terraces due to the continued oxygen attack along the step edge. As indicated by the white arrows in Fig. 3(a), the number density and size of depressions in the CuAu-terminated terraces also increase upon the increased O$_2$ exposure.

Figure 3(b) shows the STM height profile taken along the white dashed line across terraces X, Y, and Z in Fig. 3(a). The step height of $\sim$1.73 Å corresponds to the monoatomic step between the upper CuAu(100)-terminated terrace (X) and

the lower Cu(100)-terminated, $c(2 \times 2)$-O terrace (Y), and the step height of $\sim$2.01 Å is commensurate with the monoatomic step between the upper Cu(100)-$c(2 \times 2)$-O terrace (Y) and the lower CuAu terrace (Z), consistent with the STM surface profiles shown in Fig. 2. This is further confirmed by the atomically resolved STM image. As shown in Fig. 3(c), the zoomed-in STM image of the region marked with white dashed box c in Fig. 3(a) illustrates the $c(2 \times 2)$-O superstructure formed on the Cu-terminated terrace. Figure 3(d) is an atomically resolved STM image of the stepped region, as marked with white dashed box d in Fig. 3(a), in which the bright dots can be assigned as O atoms because the STM image was obtained using the same tunneling conditions as that for imaging the $c(2 \times 2)$-O superstructure within the terrace [Fig. 3(c)]. The consideration of bright dots as O is further confirmed by the STM height profile taken along the step edge across the bright dots in Fig. 3(d). As shown in Fig. 3(e), the distance between the adjacent O atoms is $\sim$3.60 Å, and the surface corrugation value is close to $\sim$0.16 Å, which also matches that in the $c(2 \times 2)$-O structure. Although the zigzag edges tend to be defective and short, the STM observation reveals that O atoms are still adsorbed into the hollow sites of the Cu atoms along the step edge region of the Cu-terminated terrace, as shown schematically by the overlaid atomic structure in Fig. 3(d).

Figure 4 corresponds to the longer O$_2$ exposure (1800 L) that results in the significant area shrinkage of CuAu-terminated terraces. As marked in Fig. 4(a), the extension of the lateral size of the oxygenated Cu terraces increases up to $\sim$80 nm, while the CuAu terraces shrink in size to as small as $\sim$5 nm in some regions. Meanwhile, Fig. 4(a) also shows that the oxygenated Cu terraces have a high density of clusters, whereas the CuAu terraces are relatively free of clusters. As marked by the arrows, long and thin strips are also formed in the oxygenated Cu terraces. Figure 4(b) displays
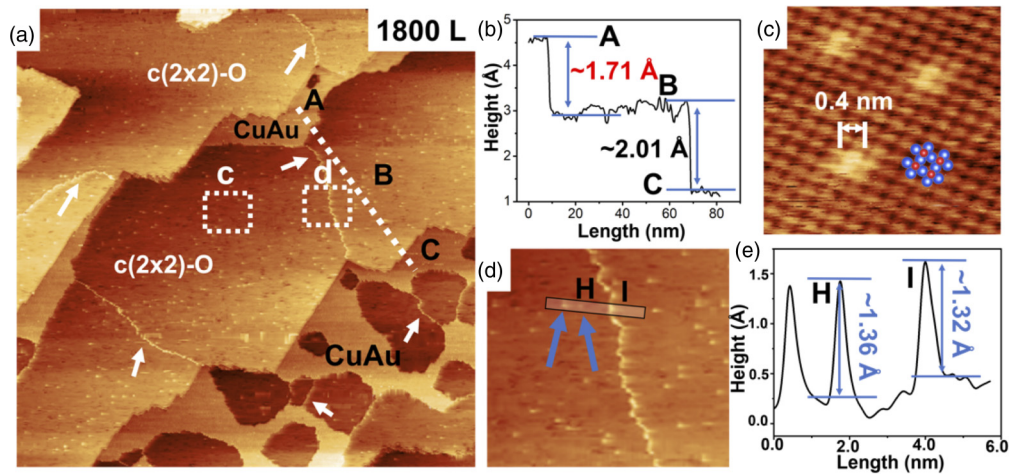
FIG. 4. (a) Scanning tunneling microscopy (STM) image (size: $300 \times 300 \, nm^2$) of the $Cu_3Au(100)$ surface after 1800 L of O_2 exposure at 350 °C. (b) STM line profile along the white dashed line across the oxygenated Cu terrace (B) and its upper and lower oxygenated Cu terraces (A, C) in (a). (c) Atomically zoomed-in STM image (size: $3 \times 3 \, nm^2$) of the oxygenated Cu terrace marked with white dashed box c in (a), showing the formation of Cu clusters on the Cu-terminated $c(2 \times 2)$-O surface. (d) Zoomed-in STM image (size: $40 \times 40 \, nm^2$) of the region consisting of a Cu strip and Cu clusters, as marked with white dashed box d in (a). (e) STM line profile across the Cu strip and Cu clusters as marked by the thin rectangle in (d), showing their similar surface heights of ~1.3 Å. The tunneling conditions for STM imaging: (a) and (d) $V_B = 2 \, V$, $I_T = 0.1 \, nA$, and (c) $V_B = 0.1 \, V$, $I_T = 1 \, nA$.

the STM height profile along the white dashed line across an oxygenated Cu terrace and its upper and lower CuAu terraces in Fig. 4(a), where the step heights of ~1.71 and ~2.01 Å are consistent with the monatomic step heights between the upper CuAu terrace (A) and the wide lower oxygenated Cu terrace and the monatomic step between the oxygenated Cu terrace (B) and the bottom CuAu terrace (C), respectively. Figure 4(c) shows an atomically zoomed-in STM image of the region marked with white dashed box c in Fig. 4(a), which confirms the $c(2 \times 2)$-O superstructure formed in the oxygenated Cu terrace. Clusters with a lateral size of ~4 Å are also visible in the STM image, and the surface height of clusters are revealed later by the STM line profile [Fig. 4(e)].

Figure 4(d) shows a zoomed-in STM image of the region with a long strip in the $c(2 \times 2)$-O oxygenated Cu terrace, as marked with white dashed box d in Fig. 4(a). The atomic structure of these long bright strips cannot be resolved clearly from the STM image. Figure 4(e) illustrates the STM height profile across the strip and clusters, as marked by the thin rectangle in Fig. 4(d), showing a similar surface height of ~1.34 ± 0.02 Å for the cluster (H) and strip (I). The similar surface heights of the strips and clusters suggest that they are composed of the same type of atomic species. As elucidated later by XPS analysis in Fig. 6 and DFT modeling in Fig. 9, these strips and clusters are composed of Cu atoms and formed via the aggregation of Cu adatoms generated from O-attack-induced decomposition of the CuAu terraces (the decomposition of the CuAu terraces also results in Au adatoms that dissolve in the bulk because of the lack of oxygen affinity for Au). The absence of the clusters on the CuAu terraces indicates that Cu adatoms prefer to stay on the $c(2 \times 2)$-O terraces rather than on the CuAu terraces due to the anchoring effect from the adsorbed O on stabilizing the clusters of Cu adatoms.

Figure 5(a) displays an STM image of the surface morphology after 2400 L of the O_2 exposure. Compared with the lower

O_2 exposures shown above, the surface now has improved smoothness with the more straightened morphology of the step edges. Meanwhile, the number density of Cu clusters is significantly reduced, but with an increased average size. As indicated by white arrows, each terrace has long bright strips of Cu adatoms, suggesting nearly complete decomposition of all the CuAu terraces, thereby transforming almost the entire surface to the oxygenated Cu termination. This is confirmed by the atomically zoomed-in STM image [the bottom-left inset of Fig. 5(a)], showing the formation of the $c(2 \times 2)$-O superstructure by O adsorption into the hollow sites of the Cu terraces. The upper-left corner region (marked with the black arrow) shows a very small terrace, which is a reminder of the undecomposed CuAu terrace. The decomposition of the CuAu terraces also transforms the monatomic steps between adjacent CuAu and Cu terraces into bilayer atomic steps. This is confirmed by measuring the step heights across the different terraces in Fig. 5(b), where the surface profile is obtained along the black dashed line in Fig. 5(a). All the steps now have the surface height of ~3.81 ± 0.04 Å, which is the sum of the heights of monatomic steps shown in Figs. 2–4.

Figure 5(c) is an atomically resolved STM image of the oxygenated Cu terrace, as marked with white dashed box c in Fig. 5(a), confirming the presence of Cu clusters on the $c(2 \times 2)$-O surface. The upper-right inset of Fig. 5(a) is a line profile across the Cu cluster marked by the black dashed line, showing a surface height of ~1.90 Å and a lateral size of ~1.1 nm. Figure 5(d) shows a zoomed-in STM image of the region containing several strips in the $c(2 \times 2)$-O terrace, as marked with white dashed box d in Fig. 5(a). Figure 5(e) is the STM line profile along the white dashed line across two strips (H, I) marked in Fig. 5(d), showing the strip heights of ~1.60 ± 0.04 Å, which are ~0.3 Å higher than the surface height (~1.34 Å) of the strips for the shorter time of the O_2 annealing [Fig. 4(e)]. As opposed to the lower O_2 exposures, the increased sizes (both laterally and vertically) of the clusters
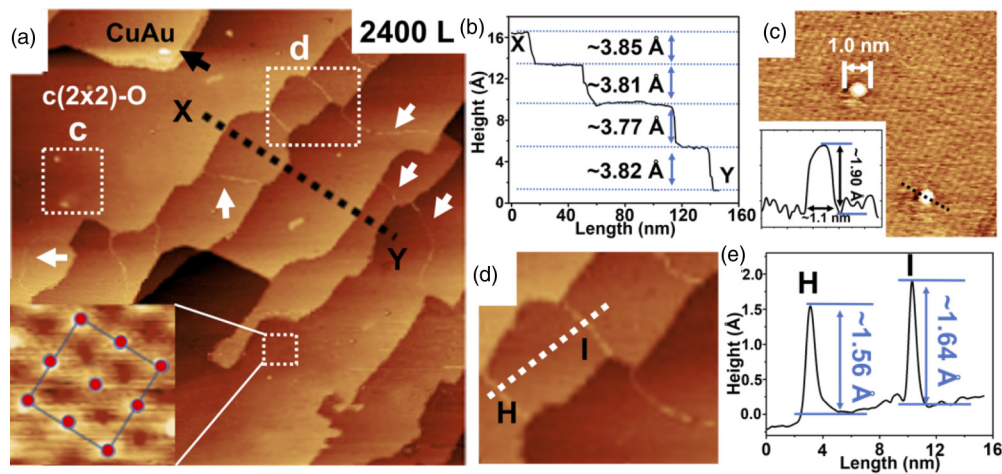
FIG. 5. (a) Scanning tunneling microscopy (STM) image (size: $300 \times 300 \, \mathrm{nm}^2$) of the $\mathrm{Cu_3Au}(100)$ surface after 2400 L of $\mathrm{O_2}$ exposure at $350\,^\circ\mathrm{C}$. The white arrows mark the formation of Cu strips in the oxygenated Cu terraces. The black arrow marks the remaining, undecomposed CuAu terrace. The bottom-left inset is an atomically zoomed-in STM image (size: $1.5 \times 1.5 \, \mathrm{nm}^2$) of the oxygenated Cu terrace, overlaid onto the STM image is the $c(2 \times 2)$-O superstructure. (b) STM line profile along the black dashed line across the multiple terraces in (a). (c) Zoomed-in STM image (size: $10 \times 10 \, \mathrm{nm}^2$) of the region with Cu clusters, as marked with white dashed box c in (a). The bottom-left inset is the surface height profile along the black dashed line across a Cu cluster. (d) Zoomed-in STM image (size: $20 \times 20 \, \mathrm{nm}^2$) of the region with Cu strips, as marked with white dashed box d in (a). (e) STM surface profile along the white dashed line across Cu strips H and I in (d), showing their similar surface heights of $\sim$1.5 and $\sim$1.6 Å, respectively. The tunneling conditions for STM imaging: (a) and (d) $V_B = 1.5 \, \mathrm{V}$, $I_T = 0.1 \, \mathrm{nA}$, and (c) $V_B = 0.1 \, \mathrm{V}$, $I_T = 1 \, \mathrm{nA}$.

and strips are induced by a three-dimensional ripening process of Cu adatoms during the prolonged $\mathrm{O_2}$ annealing, which results in fewer but larger clusters, as shown in Fig. 5(a). STM imaging of the $\mathrm{Cu_3Au}(100)$ surface after the $\mathrm{O_2}$ exposure at $100\,^\circ\mathrm{C}$ shows similar behavior of the oxygen-adsorption-induced decomposition of the topmost CuAu plane (data not shown), albeit with slower kinetics.

B. AP-XPS measurements

To complement the above STM observations that provide microscopic information on the surface morphology and atomic structure changes induced by the oxygen attack, AP-XPS is employed to monitor the temporal evolution of surface composition and chemical state during the $\mathrm{O_2}$ exposure. As shown in Fig. 6(a), the Au $4f$ region of the XPS spectra obtained from the pristine $\mathrm{Cu_3Au}(100)$ (under UHV) consists of Au $4f_{7/2}$ and Au $4f_{5/2}$, each of which can be deconvoluted into two components, located at the binding energies of 84.0 and 83.5 eV for Au $4f_{7/2}$ and 87.5 and 87.0 eV for Au $4f_{5/2}$, respectively. As marked in Fig. 6(a), the two components correspond to surface (S) Au and bulk (B) Au, and their binding energies are consistent with previous work on the Cu-Au alloys [12,20,32,33]. Figure 6(a) illustrates that the peak intensity of the surface Au component decreases gradually upon the continued exposure of the $\mathrm{Cu_3Au}(100)$ to $p\mathrm{O_2} = 1 \times 10^{-6}$ Torr and $350\,^\circ\mathrm{C}$. After $\sim$40 min of the $\mathrm{O_2}$ exposure, the surface Au peak disappears completely. By contrast, the bulk Au component only has a slight increase in the peak intensity, and its binding energy remains the same at 84 eV. This is further evident from the temporal evolution of the integrated intensities of the surface Au and bulk Au peaks in Fig. 6(b), which shows that the peak intensity for surface Au drops quickly while the peak intensity of bulk Au only

increases slightly and then reaches a saturated level during the continued $\mathrm{O_2}$ exposure. As illustrated from the STM imaging in Figs. 2–5, the O adsorption leads to the decomposition of CuAu terraces, which results in Cu and Au adatoms. As shown here by the XPS measurements, the complete disappearance of the surface Au peak reveals that Au adatoms actually dissolve into the bulk, and the surface clusters observed in the STM images (Figs. 3–5) are formed by the aggregation of Cu adatoms supplied from the decomposing CuAu terraces. Meanwhile, the relatively constant intensity of the bulk Au peak indicates that Au travels into the deeper subsurface region. Meanwhile, the $\mathrm{O_2}$-induced surface termination of Cu is further confirmed by XPS measurements with different incident photon energies. As shown in Fig. 6(c), the Au $4f$ and Cu $3p$ region taken with the lower photon energy of 400 eV shows the absence of Au $4f$ signal, suggesting that the top surface is terminated as nearly pure Cu. The Au $4f$ peak emerges stronger in intensity with the higher photon energies of 1150 and 1250 eV, indicating the higher Au concentration in the deeper subsurface region.

The oxygen-attack-induced decomposition of CuAu-terminated terraces is corroborated by monitoring the corresponding O $1s$ spectra as a function of the $\mathrm{O_2}$ exposure [Fig. 6(d)]. The pristine surface is O free, as confirmed by the absence of any detectable intensity from the O $1s$ region under UHV [the bottom panel in Fig. 6(d)]. Exposure to $p\mathrm{O_2} = 1 \times 10^{-6}$ Torr and $350\,^\circ\mathrm{C}$ (same as the STM experiments above) results in appreciable intensity in the O $1s$ core level, indicating the O uptake by chemisorption that results in the $c(2 \times 2)$-O superstructure on Cu-terminated terraces, as shown by the above STM imaging (Figs. 2–5). Figure 6(e) corresponds to the evolution of the integrated intensities of the O $1s$ spectra as a function of the $\mathrm{O_2}$ exposure time. By combining the STM imaging shown in Figs. 2–5, it can be known
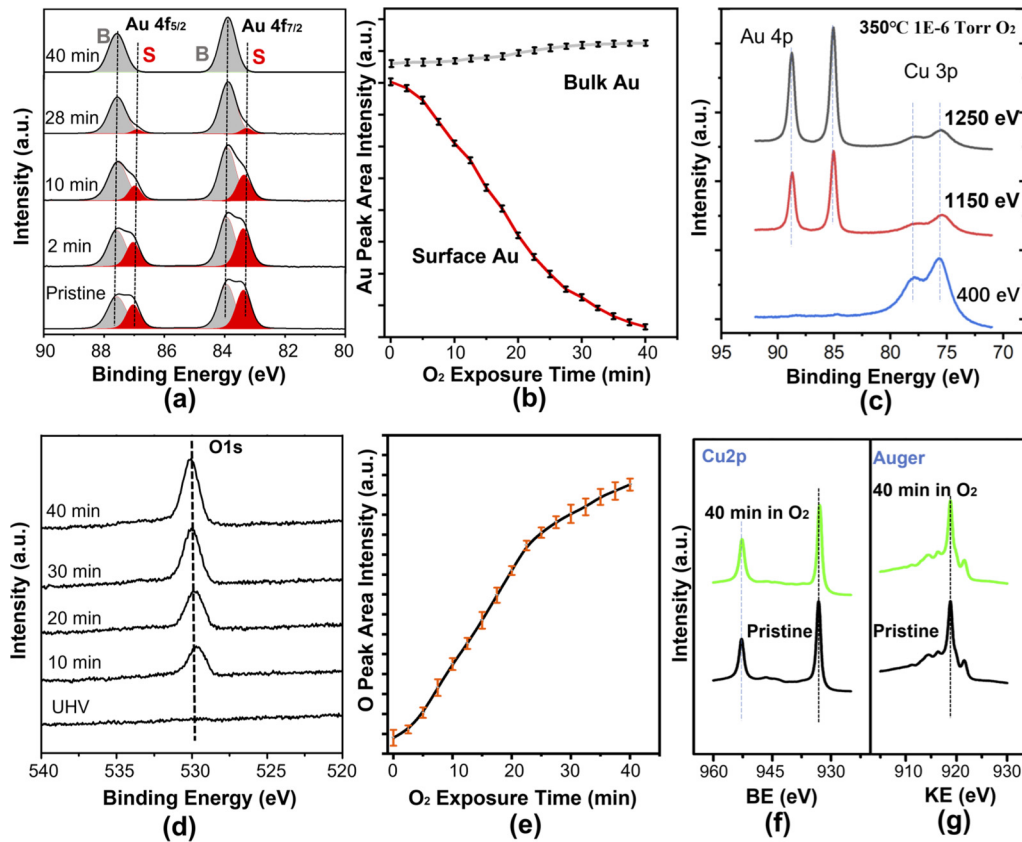
FIG. 6. (a) Temporal evolution of Au-4f x-ray photoelectron spectroscopy (XPS) spectra taken with the incident photon energy of 400 eV during the exposure of the Cu$_3$Au(100) at 350 °C to pO$_2 = 1 \times 10^{-6}$ Torr. S (in red) and B (in gray) correspond to the surface Au and bulk Au contributions, respectively. (b) Evolution of the integrated area of the surface Au and bulk Au peaks as a function of O$_2$ exposure time. (c) Au 4f and Cu 3p spectra of the Cu$_3$Au(100) measured at 350 °C and pO$_2 = 1 \times 10^{-6}$ Torr with the incident photon energies of 400, 1150, and 1250 eV, respectively. (d) Temporal evolution of O 1s spectra taken with the incident photon energy of 650 eV during the exposure of the Cu$_3$Au(100) at 350 °C to pO$_2 = 1 \times 10^{-6}$ Torr. (e) Integrated intensities of the O 1s spectra during the continued O$_2$ exposure. (f) and (g) Cu 2p and Cu L$_3$M$_{45}$M spectra confirming the metallic state of Cu during the O$_2$ dosing.

that the continued increase in the O 1s intensity is caused by the $c(2 \times 2)$-O formation on Cu-terminated terraces and the O-attack-induced decomposition of CuAu terraces, where the latter results in the formation of monatomic depressions with the $c(2 \times 2)$-O formation on the exposed Cu plane of the bottom of the surface pits. Figures 6(d) and 6(e) show that continued O$_2$ exposure brings stronger intensity to the O 1s spectra but does not induce noticeable changes in the peak position, confirming that the oxidation condition (pO$_2$, T) employed here allows for building up more chemisorbed O on the surface but is not sufficient to drive the transformation of the $c(2 \times 2)$-O to other O chemisorbed phases (such as the $(2\sqrt{2} \times \sqrt{2})R45°$-O missing-row reconstruction) or bulk oxide formation, as observed from the oxidation pathway of Cu(100) [13,29,34–36]. The surface oxidation not going beyond $c(2 \times 2)$-O is also confirmed by the coordinated Cu 2p [Fig. 6(f)], where the shape and position of the Cu 2p core level peaks remain the same for the pristine and the O$_2$-exposed surfaces, indicating that Cu remains its metallic state. This is further corroborated by the Cu L3M$_{45}$M$_{45}$ Auger spectra that are also acquired to confirm the valence states of Cu, as shown in Fig. 6(g). The pristine Cu$_3$Au(100) surface shows the Cu LMM line peak at a kinetic energy (KE) of 918.6 eV, which is associated with metallic Cu^0. The subsequent

O$_2$ exposure at pO$_2 = 1 \times 10^{-6}$Torr and 350 °C results in no changes in the line position and shape of the Cu LMM spectra. The combined STM, XPS, and Auger measurements confirm that Cu largely maintains its metallic state (Cu^0), although the surface is covered with chemisorbed O.

C. LEIS measurements

To complement the XPS measurements of the surface composition averaged over a few atomic layers (i.e., the thickness corresponding to the mean free path of photoelectrons), LEIS is also performed to monitor the O-adsorption-induced composition evolution in the topmost atomic layer only. The LEIS spectra are taken with 1499 eV He$^+$ and the scattering angle of 135°, under which a good mass separation between Au and Cu can be ensured in combination with a high detector efficiency. We firstly measure the ISS spectra from pure Cu and pure Au samples to obtain the elemental sensitivity factors. The elemental sensitivity factor does not depend on the chemical environment of an atom in the surface [37]. The surface composition of the Cu$_3$Au(100) can be directly quantified with the ISS peak intensities modified by the sensitivity factor of Cu and Au. Figure 7(a) shows the LEIS spectra, in which the three peaks located at KE = 626, 1209, and 1399 eV
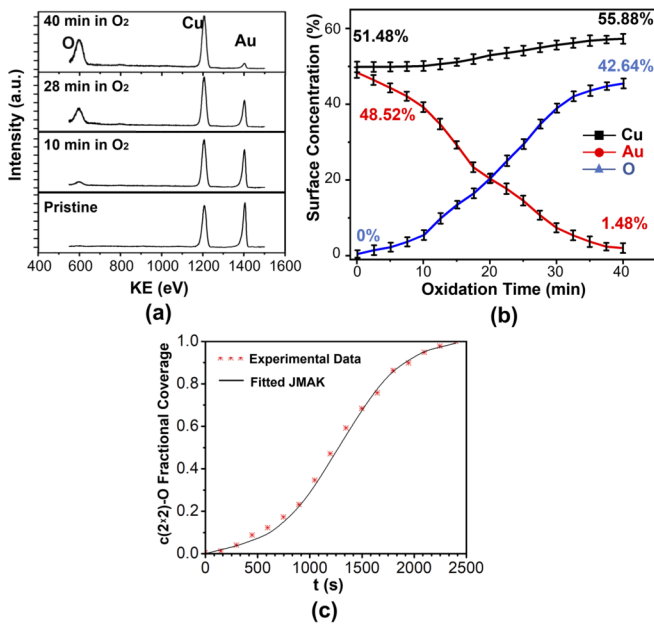
FIG. 7. (a) Temporal evolution of low-energy ion scattering (LEIS) spectra obtained from the Cu$_3$Au(100) during the exposure of the Cu$_3$Au(100) at 350 °C to pO$_2$ = 1 × 10^{-6} Torr. (b) Evolution of the composition of Au, Cu, and O in the topmost surface layer as a function of the O$_2$ exposure time. (c) Evolution of the $c(2 \times 2)$-O fractional area coverage as a function of the O$_2$ exposure time, and its fit to the JMAK equation $X(t) = 1 - \exp(-kt^n)$, where $n = 2$, and $k = 3.8 \times 10^{-7}$ s^{-2}.

correspond to O, Cu, and Au, respectively. For the pristine surface under UHV, there is no detectable O signal, and the Cu and Au peaks show similar intensity. Upon switching from the UHV to O$_2$ gas at pO$_2$ = 1 × 10^{-6} Torr and 350 °C, the O peak becomes visible, and its intensity increases with the continued O$_2$ exposure. By contrast, the intensity of the Au peak decreases and becomes nearly invisible after ~40 min of the O$_2$ exposure.

Figure 7(b) illustrates the surface composition evolution by quantifying the integrated peak areas of O, Cu, and Au in the LEIS spectra modified by corresponding atomic sensitive factor in Fig. 7(a), showing that the O concentration increases, whereas the Au concentration decreases as a function of the O$_2$ exposure. This indicates an increased O amount whereas a decreased net amount of Au in the topmost surface with the continued O$_2$ exposure, consistent with the trend derived from the XPS measurements in Fig. 6. It can be also noted from Fig. 7(b) that the Cu composition is slightly higher than the Au composition for the pristine surface, which is consistent with the STM observation showing that the pristine surface is dominated by CuAu terraces (consisting of equal numbers of Cu and Au atoms) along with narrow terraces having the surface termination of the pure Cu plane (Fig. 1). Figure 7(b) also shows that the Cu concentration increases from ~52% in the beginning to ~56% at the end of the O$_2$ exposure (~40 min), corroborating well with the STM observations (Figs. 3–5) of Cu clusters and strips formed by the aggregation of Cu adatoms supplied from decomposing CuAu terraces. Meanwhile, the decreased Au concentration

and its disappearance at the end also confirm the dissolution of Au adatoms from the decomposing CuAu terraces into the bulk of the Cu$_3$Au crystal.

D. Johnson-Mehl-Avrami-Kolmogorov fit of the oxygen chemisorption kinetics

The O chemisorption on the Cu$_3$Au(100) occurs via a nucleation and growth process. This is evidenced by the formation and growth of monatomic depressions of $c(2 \times 2)$-O domains in CuAu terraces from our STM observations (Figs. 2–5). This is also consistent with previous studies suggesting the nucleation and growth mechanism for oxygen-chemisorption-induced surface phase transformations on the Cu(110) surface [38,39]. Kinetics of the phase transformations that occur via nucleation and growth is commonly addressed through the classic theory of Johnson-Mehl-Avrami-Kolmogorov (JMAK) [40,41]. For phase transformations in two-dimensional (2D) systems (like surfaces), the JMAK theory assumes that the fractional coverage of the transformed area $X(t)$ follows an exponential dependence on time t:

$$X(t) = 1 - \exp(-kt^n), \qquad (2)$$

where n is the Avrami exponent, and k is the reaction rate constant. The Avrami exponent contains information about nucleation mechanisms and growth dimensionality (D). Nucleation mechanisms can be categorized based on how frequent nucleation occurs in the system. If the formation of nuclei happens only at the beginning of the transformation period and growth takes place afterwards, it would then be identified as site-saturated nucleation, and $n = D$. By contrast, if the system keeps adding nuclei with a constant rate over the entire transformation period, it would be characterized as the constant nucleation rate mechanism, and $n = D + 1$. The rate constant, on the other hand, is computed as $k = \pi v^2 N$ for site-saturated nucleation and $k \sim \pi v^2 \dot{N}$, where N is nucleation density, $\dot{N}$ constant nucleation rate, and v the constant interface velocity.

The evolution of the $c(2 \times 2)$-O fractional area coverage can be obtained using the LEIS-measured surface composition of O shown in Fig. 7(b) and by calibrating against the O concentration at the saturated $c(2 \times 2)$-O coverage (= 1). Figure 7(c) shows the plot of the $c(2 \times 2)$-O fractional area coverage with respect to the O$_2$ exposure time. The solid line is the best fit to the JMAK equation [Eq. (2)], where $n = 2$, $k = 3.8 \times 10^{-7}$ s^{-2}. Based on the $c(2 \times 2)$-O fractional area coverage evolution [Fig. 7(c)], we can present a physical picture of nucleation and growth for linking the STM imaging (Figs. 2–5) to the JMAK fitting parameters. The Avrami exponent value $n = 2$ obtained from the JMAK fitting indicates a site-saturated nucleation mechanism of $c(2 \times 2)$-O, which corroborates well with the STM results. As shown in Fig. 1, the pristine Cu$_3$Au(100) surface consists of wide CuAu terraces and narrow Cu terraces. After 200 L of O$_2$ exposure, the surface is oxidized into the $c(2 \times 2)$-O for the Cu terraces and depressions within the CuAu terraces. Therefore, the nucleation density of $c(2 \times 2)$-O can be determined by counting the number density of Cu terraces and depressions in the STM images. As shown in Figs. 2–5, the surface

densities of $c(2 \times 2)$-O nuclei can be determined as $N = 3.6 \times 10^{-4} \, \text{nm}^{-2}$, $4.0 \times 10^{-4} \, \text{nm}^{-2}$, and $3.9 \times 10^{-4} \, \text{nm}^{-2}$ for the O$_2$ exposures of 200, 800, and 1800 L, respectively. This indicates that the $c(2 \times 2)$-O nucleation happens only at the beginning of the O$_2$ exposure, and the continued O$_2$ exposure only leads to the growth of nucleated $c(2 \times 2)$-O domains. This site-saturated nucleation behavior suggests a surface diffusion mechanism of oxygen that results in an active zone of capture of oxygen around each $c(2 \times 2)$-O nucleus. That is, oxygen landing inside this capture zone may migrate to the $c(2 \times 2)$-O nucleus, leading to the growth of the $c(2 \times 2)$-O nucleus rather than nucleating a new $c(2 \times 2)$-O cluster. Therefore, there is a saturated number density of $c(2 \times 2)$-O clusters due to the competition for the capture of diffusing O on the surface. Meanwhile, we can also obtain experimentally the value of the fit parameter of the rate constant $k = (\pi)v^2 N$ from the analysis of the STM imaging of nucleation and growth of $c(2 \times 2)$-O clusters. As measured from the STM images in Figs. 2–5, the values for the saturated nucleation density and the constant interface velocity can be determined as $N = \sim 3.83 \times 10^{-4} \, \text{nm}^{-2}$ and $v = \sim 8.6 \times 10^{-2} \, \text{nm s}^{-1}$ (by approximating a circular shape of the $c(2 \times 2)$-O clusters). Therefore, the rate constant k has the value of $k = 3.31 \times 10^{-7} \, \text{s}^{-2}$ which matches very well with that ($k = 3.8 \times 10^{-7} \, \text{s}^{-2}$) from the JMAK fitting in Fig. 7(c). This excellent agreement between the experiments (STM and LEIS) and the JMAK fitting demonstrates that the surface diffusion of oxygen is the dominant mechanism underlying the experimentally observed site-saturated nucleation and 2D growth kinetics of $c(2 \times 2)$-O domains.

E. DFT modeling

The experiments and analysis shown above demonstrate that the initial oxidation of Cu$_3$Au(100) begins with the nucleation and growth of $c(2 \times 2)$-O domains. Figure 8 schematizes the key feature of the microscopic processes as identified from STM observations. The pristine surface consists of narrow Cu terraces and wide CuAu terraces, which are separated by single-atomic-height steps [Fig. 8(a)]. The O adsorption results in the nucleation of $c(2 \times 2)$-O domains on the Cu terraces and within the CuAu terraces by locally decomposing the topmost CuAu layer, thereby exposing the underlying Cu plane and forming monatomic depressions [Fig. 8(b)]. The continued O$_2$ exposure leads to the growth of $c(2 \times 2)$-O domains via the receding motion of the monatomic steps of CuAu terraces [Fig. 8(c)]. The O-adsorption-induced decomposition of the CuAu terraces transforms the entire surface into Cu(100)-like, $c(2 \times 2)$-O terminated terraces separated by double-atomic-height steps [Fig. 8(d)]. Although the above microscopic processes are revealed from the STM observations, two questions naturally arise as to (i) why monatomic CuAu steps undergo receding motion to expose the underlying Cu plane and (ii) how monatomic depressions form within CuAu terraces, both of which require decomposing CuAu terraces. We attribute the CuAu decomposition to O adsorption along the step edge and within the CuAu terraces, which results in the abstraction of Cu and Au atoms surrounding the adsorbed O.
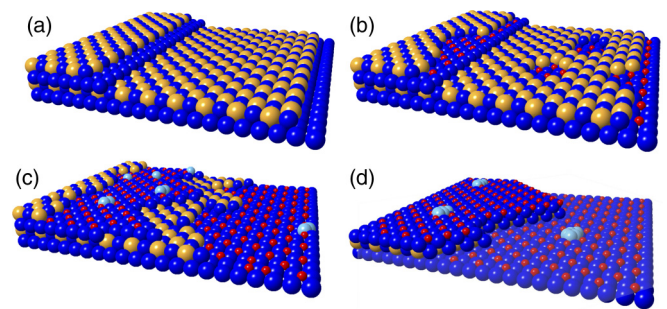

FIG. 8. Schematic illustrations showing the microscopic processes of the initial-stage oxidation of Cu$_3$Au(100). (a) Pristine Cu$_3$Au(100) consisting of wide CuAu terraces and narrow Cu terraces separated by monoatomic steps. (b) O$_2$ exposure results in the nucleation of $c(2 \times 2)$-O domains by O adsorption into fourfold hollow sites of Cu terraces and O-adsorption-induced formation of surface pits in CuAu terraces. (c) The growth of $c(2 \times 2)$-O domains occurs via O-adsorption-induced decomposition of CuAu terraces via the receding motion of atomic steps, which results in Cu adatoms (aggregating into Cu clusters) and Au adatoms (dissolving into the bulk). (d) O adsorption induced complete decomposition of CuAu terraces transforms the entire surface into Cu(100)-like, $c(2 \times 2)$-O terminated terraces separated by double-atomic-height steps along with the formation of Cu clusters on the surface. Yellow, blue, and red balls represent Au, Cu, and O atoms, respectively, and light blue balls stand for Cu adatoms.

To further substantiate the O adsorption effect on the CuAu decomposition, we employ DFT computation to evaluate the relative stability of Cu and Au atoms in the vicinity of adsorbed O along the step edge and on the CuAu terrace. As known from the STM images in Figs. 1–6, the preferred terrace edge orientation is along the [110] direction. Figure 9(a) shows the atomic structure of the [110] step consisting of the lower Cu(100) terrace and the upper CuAu(100) terrace. There are three crystallographically nonequivalent fourfold hollow sites for O adsorption along the step edge, marked as 1, 2, and 3 in Fig. 9(a). The O adsorption energies for these three sites are calculated to be -1.89, -1.71, and -0.92 eV, respectively. Therefore, site 1, which has five coordinating Cu atoms (four in the Cu terrace and one beneath), is energetically most favorable for O adsorption because of the larger O affinity of Cu than Au. The presence of the adsorbed O at site 1 also promotes the step-edge detachment of the adjacent Au on the upper terrace, as marked by the white dashed circle in Fig. 9(b). This is confirmed by DFT computations showing the significant decrease in the vacancy formation energy of the step-edge Au atom from 0.74 eV (before the O adsorption) to 0.36 eV (after the O adsorption), which is lower enough for the Au atom to detach from the step edge at the elevated temperature of the experiment (350 °C). In the same way, another O atom is adsorbed into the nearest equivalent fourfold hollow site that also has five coordinating Cu atoms, thereby inducing the step-edge detachment of the Au atom on the upper terrace, as shown in Fig. 9(c). Upon the departure of the two Au atoms, the step-edge Cu atom, as marked by the white dashed circle in Fig. 9(c), becomes significantly undercoordinated and detaches spontaneously from the step edge (with the vacancy formation energy of -0.14 eV). The
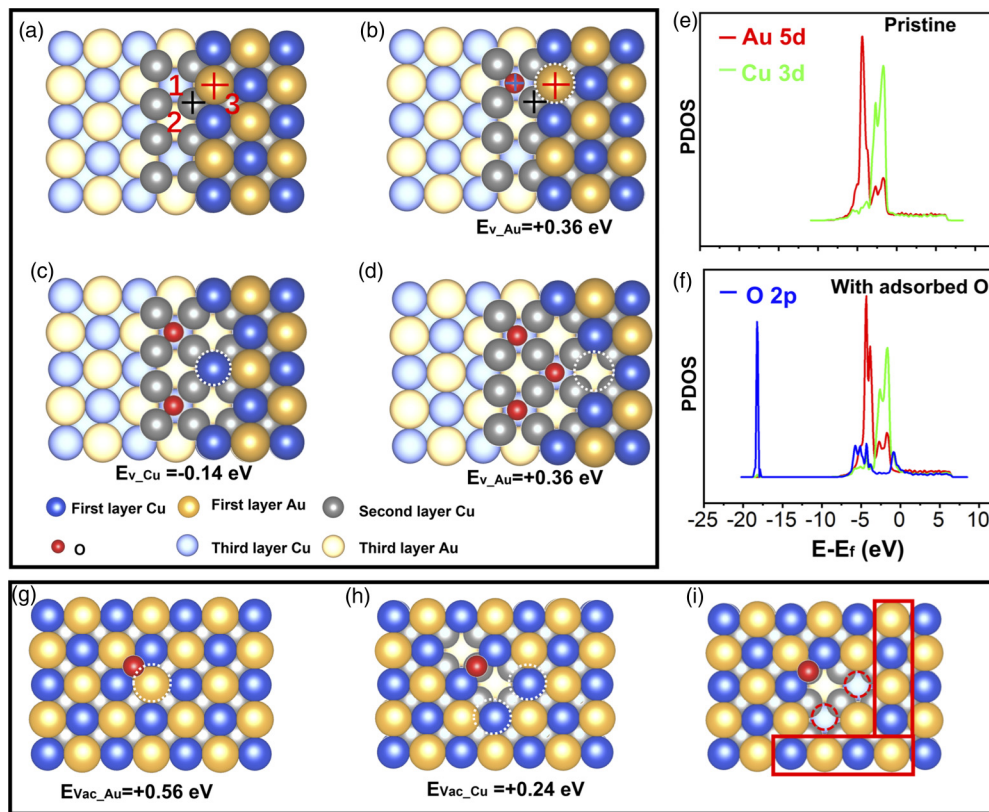
FIG. 9. Density functional theory (DFT) modeling of O-adsorption-induced AuCu decomposition via step-edge and in-terrace detachment. (a) Stepped $Cu_3Au(100)$ surface consisting of Cu-terminated and CuAu-terminated terraces separated by monatomic steps with the terrace edge orientation along the [110] direction. Three crystallographically nonequivalent fourfold hollow sites are identified for O adsorption in the vicinity of the step edge. (b) O preferentially adsorbs at hollow site 1 consisting of five coordinating Cu atoms, destabilizing the adjacent Au atom (marked by the white dashed circle) on the upper terrace. (c) The departure of the second Au atom induces the adsorption of another O at the adjacent equivalent hollow site of the Cu terrace and results in the spontaneous detachment of the Cu atom (marked by the white dashed circle) from the step edge. (d) The continued O adsorption at the equivalent hollow sites along the step edge results in the extension of the Cu terrace. (e) PDOS of Cu $3d$ and Au $5d$ for the pristine step in (a). (f) PDOS of Cu $3d$, Au $5d$, and O $2p$ of the step with an adsorbed O atom in (b). (g) O adsorbs at the bridge site consisting of three coordinating Cu atoms and two coordinating Au atoms, destabilizing the adjacent Au atom (marked by the white dashed circle). (h) The departure of the Au atom in the CuAu terrace results in the spontaneous detachment of the Cu atoms (marked by the white dashed circles). (i) The departure of the two Cu atoms results in the formation of two [110] steps (marked with the red rectangles) that are like the step configuration in (a), where the two fourfold hollow sites (marked by red dashed circles) are subjected to O adsorption to form the $c(2 \times 2)$-O structure.

O-adsorption-induced step-edge detachment of the Au and Cu atoms exposes the underlying Cu plane, and this leads to the extension of the lower Cu terrace by the same way of adsorbing O atoms as the similar fourfold hollow sites with five coordinating Cu atoms [Fig. 9(d)].

The O-adsorption-induced step-edge detachment is further elucidated by the projected density of states (PDOS) of the $3d$ and $5d$ orbitals of the Cu and Au atoms and O $2p$ of chemisorbed O. As shown in Fig. 9(e), the Cu $3d$ band overlaps with the Au $5d$ band below the Fermi level, indicating the Cu $3d$-Au $5d$ hybridization for the pristine step [Fig. 9(a)]. Figure 9(f) corresponds to the PDOS plots obtained from the step with adsorbed O adjacent to the Au atom [Fig. 9(b)], showing the hybridization between Cu $3d$ and O $2p$ at -19 eV and near the Fermi level region. Compared with the pristine step, the density states of Cu $3d$ decrease in the Cu $3d$-Au $5d$ hybridization region, and the broadening of the Cu $3d$

band results in a tiny density shoulder near the Fermi level to overlap with O $2p$, indicating the weakening of the Cu-Au bond because of the decreased charge transfer from Cu to Au. This is also confirmed by the Bader charge analysis of the pristine and O adsorbed steps. The Cu and Au atoms within the pristine step have the Bader charges of 10.89e and 11.35e, respectively. The O adsorption at the step edge [Fig. 9(b)] results in a large decrease in the Bader charge of the Cu atom to 10.66e but a smaller increase (11.31 eV) by the Au atom. This indicates the increased electron transfer from Cu to O but decreased electron gain by Au.

We then examine O-adsorption-induced pit formation in the CuAu terrace. Figure 9(g) shows the CuAu terrace, in which the fourfold hollow site is found to be more favorable than the neighboring bridge site for O adsorption. The presence of adsorbed O at the hollow site promotes the abstraction of the adjacent Au from the terrace, as marked by

the white dashed circle in Fig. 9(g). This is shown by the change in the vacancy formation energies of the Au atom, which are calculated to be 0.94 and 0.56 eV before and after the O adsorption. Upon the abstraction of the Au atom, the adjacent Cu atoms, as marked by the white dashed circle in Fig. 9(h), become undercoordinated, and their small vacancy formation (0.24 eV) makes these Cu atoms readily detach from the surface at the elevated temperature of the experiment. The O-adsorption-induced departure of the Au and Cu atoms results in a ML pit in the CuAu terrace and thus exposes the underlying Cu plane. As marked by the red solid rectangles in Fig. 9(i), the Cu-Au-Cu rows adjacent to the surface pit locally have the same step-terrace configuration as that in Fig. 9(b), and the hollow sites marked with the red dashed circles have five coordinating Cu atoms and thus are more favorable for O adsorption. In the same manner as shown in Figs. 9(b)–9(d), O adsorption at these hollow sites of the exposed Cu plane significantly destabilizes the Au and Cu atoms along the step edge. The continued O adsorption results in the exfoliation of the CuAu layer along with the nucleation and growth of the $c(2 \times 2)$-O on the exposed Cu plane, as shown in our STM images (Figs. 2–5). As also shown from our STM observations, the $Cu_3Au(100)$ consists of a high density of steps and terraces, and oxygen-adsorption-induced decomposition of the topmost CuAu layer tends to happen more readily from the steps. This is consistent with DFT calculations, showing that the CuAu decomposition from the terraces requires a larger energy barrier than that at steps.

IV. DISCUSSION

Cu-Au was studied as the simplest-possible binary alloy system (only one of the components oxidizes) for understanding the effect of the noble metal addition on the initial-stage oxidation of alloys [14,15,19,35,36,38,42–44]. For the $Cu_3Au(100)$, it was shown that O atoms preferentially adsorb at the fourfold hollow sites of the Cu-terminated surface (including the segregation of impurity O in the Cu_3Au bulk to the hollow sites of the (100) surface [31]) with no Au detected in the first layer [26,31,53,45–52]. However, the microscopic mechanism for the O-adsorption-induced formation of the Cu-terminated surface has not been identified. On one hand, our results have shown that the O_2 exposure results in the Cu-terminated $c(2 \times 2)$-O surface, which is consistent with previous studies. On the other hand, our results provide insight into the microscopic process underlying the formation of the Cu-terminated surface. Counterintuitive to the common expectations of the adsorbate-induced surface segregation of the more reactive alloy component [33,46,53–56], our observations demonstrate that the formation of the Cu surface termination occurs via the O-adsorption-induced decomposition (de-alloying) of the topmost CuAu surface layer. As shown from the STM imaging and LEED (Fig. 1), the pristine $Cu_3Au(100)$ surface is dominated by CuAu-terminated terraces separated by monatomic steps and narrow Cu-terminated terraces. The O_2 exposure results in the O-adsorption-induced decomposition of the CuAu terraces via the receding motion of the existing atomic steps as well as the nucleation of ML depressions in the CuAu terraces and their subsequent growth induced by the retraction motion of

the resultant monatomic steps. This is like the exfoliation that leads to the peeling off of the outermost CuAu layer, thereby exposing the inner Cu plane to the O attack.

The O-adsorption-induced decomposition of the topmost surface layer is like a chemical peeling procedure in which a chemical solution is applied to the surface to remove the top layers. This chemical peeling bears a clear difference from the O-adsorption-induced surface segregation, although both result in a Cu-terminated Cu surface. The O-adsorption-induced surface segregation requires counter diffusion of Au and Cu atoms between the surface and subsurface regions. That is, the surface segregation of Cu atoms from the subsurface layer is accompanied with the inward diffusion of Au atoms in the topmost layer, for which Cu is depleted from the inner layers, whereas Au is enriched in the subsurface. By contrast, the O-adsorption-induced surface peeling process itself does not require the mass exchanges between the surface and subsurface because it only involves the topmost layer, which therefore does not induce significant composition changes to the subsurface region. This is confirmed by our STM imaging (Figs. 2–5), showing the formation of Cu clusters via the aggregation of Cu adatoms supplied from the decomposing CuAu surface layer and dissolution of resulting Au adatoms into the subsurface of the Cu_3Au crystal. The latter is corroborated by the depth-resolved AP-XPS and LEIS measurements (Figs. 6 and 7), showing the absence of Au in the surface but enrichment of Au in the subsurface region during the O_2 exposure.

These fundamental insights may have practical implications. As shown above, the Cu_3Au surface can easily decompose into Cu and Au adatoms with low O_2 pressure, and the Cu adatoms subsequently aggregate into clusters along the dissolution of Au adatoms into the bulk. The Cu clusters may be oxidized into CuO_x islands upon continued O_2 exposure or with a higher oxygen chemical potential, which may serve as oxide nuclei for further oxidation. This is in line with the *in situ* electron microscopy observations showing the formation of Cu_2O islands from Cu-Au oxidation at higher O_2 pressure and temperature [57–61]. As oxidation continues, particularly at large O_2 pressures, oxide islands impinge and result in interfaces (grain boundaries) in the oxide film, which may serve as short-circuit diffusion paths for outward diffusion of Cu atoms or inward diffusion of O atoms and thus lead to poor oxidation resistance. Therefore, a control in the density of the Cu clusters in the very early stages of the oxidation may provide control over the nucleation density of the oxide islands and thus the microstructure feature of the oxide film. As shown in Figs. 2–5, the longer O_2 annealing can significantly reduce the surface density of Cu clusters. It is reasonable to expect for the further reduction in the number density of Cu clusters with a higher annealing temperature to enhance the surface diffusion of Cu adatoms.

Another case is heterogeneous catalysis that utilizes Cu and Cu alloys as catalysts for various catalytic oxidation reactions. For instance, bimetallic Cu-Au alloys have attracted considerable attention recently as improved catalysts in CO oxidation [2], propene epoxidation [62], and benzyl alcohol oxidation [63]. These catalytic reactions initiate from the surface oxidation of the alloy, where the catalytic activity depends on the surface termination, composition, atomic

structure, and morphology. As shown from our experiments and modeling, the O_2 exposure results in the decomposition of the CuAu-terminated surface layer into many single adatoms of Cu and Au (before dissolving into the bulk for the latter) and their clusters along with the O adsorption into the fourfold hollow sites of the Cu-terminated surface layer. Our results indicate that relative surface densities of these atomic species and their clustering behavior can be controlled by O_2 annealing conditions such as temperature and oxygen pressure. The interplay among these single adatoms, their clusters, and chemisorbed O may play an important role in influencing the dynamic evolution of the catalytic performance. Further investigations are needed to elucidate such interplay.

V. CONCLUSIONS

The microscopic process underlying the initial-stage oxidation of $Cu_3Au(100)$ has been investigated using a combination of surface science tools and atomistic modeling. The pristine surface consists of wide CuAu terraces and narrow Cu terraces separated by monatomic steps. The oxygen exposure induces decomposition (de-alloying) of the topmost CuAu layer via the receding motion of atomic steps and nucleation/growth of ML pits in CuAu terraces, which results in many Cu adatoms aggregating into Cu clusters and Au adatoms dissolving into the bulk. This O-adsorption-induced peeling off of the CuAu layer exposes the underlying Cu plane to the O attack. The O adsorption into the fourfold hollow sites of the exposed Cu plane results in the nucleation and growth of the $c(2 \times 2)$-O superstructure, which can be fit well by the JMAK theory with site-saturated nucleation. We expect that the present results may also be relevant to the behavior of other alloys composed of both reactive and noble components, for which the dramatic difference of the chemical reactivity of the alloying elements may drive the de-alloying at the surface.

[1] C. Bracey, P. Ellis, and G. Hutchings, Application of copper-gold alloys in catalysis: Current status and future perspectives, Chem. Soc. Rev. **38**, 2231 (2009).

[2] S. Najafishirtari, R. Brescia, P. Guardia, S. Marras, L. Manna, and M. Colombo, Nanoscale transformations of alumina-supported AuCu ordered phase nanocrystals and their activity in CO oxidation, ACS Catal. **5**, 2154 (2015).

[3] L. Luo, S. Chen, Q. Xu, Y. He, Z. Dong, L. Zhang, J. Zhu, Y. Du, B. Yang, and C. Wang, Dynamic atom Clusters on AuCu nanoparticle surface during CO oxidation, J. Am. Chem. Soc. **142**, 4022 (2020).

[4] E. Andrews, Y. Fang, and J. Flake, Electrochemical reduction of CO_2 at CuAu nanoparticles: Size and alloy effects, J. Appl. Electrochem. **48**, 435 (2018).

[5] Y. Xiao, L. Tang, W. Zhang, and C. Shen, Theoretical insights into the selective and activity of CuAu catalyst for O_2 and CO_2 electroreduction, Comput. Mater. Sci. **192**, 110402 (2021).

[6] H. Iwai, T. Umeki, M. Yokomatsu, and C. Egawa, Methanol partial oxidation on Cu-Zn thin films grown on Ni(1 0 0) surface, Surf. Sci. **602**, 2541 (2008).

[7] P. Mierczynski, K. Vasilev, A. Mierczynska, W. Maniukiewicz, R. Ciesielski, J. Rogowski, I. M. Szynkowska, A. Y. Trifonov, S. V. Dubkov, D. G. Gromov, and T. P. Maniecki, The effect of gold on modern bimetallic Au-Cu/MWCNT catalysts for the oxy-steam reforming of methanol, Catal. Sci. Technol. **6**, 4168 (2016).

[8] J. A. Rodriguez, P. Liu, J. Hrbek, J. Evans, and M. Pérez, Water gas shift reaction on Cu and Au nanoparticles supported on $CeO_2(111)$ and ZnO(0001): Intrinsic activity and importance of support interactions, Angew. Chemie - Int. Ed. **46**, 1329 (2007).

[9] S. Xia, L. Fang, Y. Meng, X. Zhang, L. Zhang, C. Yang, and Z. Ni, Water-gas shift reaction catalyzed by layered double hydroxides supported Au-Ni/Cu/Pt bimetallic alloys, Appl. Catal. B Environ. **272**, 118949 (2020).

[10] C. Li, P. Zhang, J. Wang, J. A. Boscoboinik, and G. Zhou, Tuning the deoxygenation of bulk-dissolved oxygen in copper, J. Phys. Chem. C **122**, 8254 (2018).

[11] J. Wang, D. Lu, C. Li, Y. Zhu, J. A. Boscoboinik, and G. Zhou, Measuring charge transfer between adsorbate and metal surfaces, J. Phys. Chem. Lett. **11**, 6827 (2020).

[12] C. Li, Q. Liu, J. A. Boscoboinik, and G. Zhou, Tuning the surface composition of Cu_3Au binary alloy, Phys. Chem. Chem. Phys. **22**, 3379 (2020).

[13] J. Wang, C. Li, Y. Zhu, J. A. Boscoboinik, and G. Zhou, Insight into the phase transformation pathways of copper oxidation: From oxygen chemisorption on the clean surface to multilayer bulk oxide growth, J. Phys. Chem. C **122**, 26519 (2018).

[14] M. Kittel, M. Polcik, R. Terborg, J. T. Hoeft, P. Baumgärtel, A. M. Bradshaw, R. L. Toomes, J. H. Kang, D. P. Woodruff, M. Pascal, C. L. A. Lamont, and E. Rotenberg, Structure of oxygen on Cu(1 0 0) at low and high coverages, Surf. Sci. **470**, 311 (2001).

[15] G. Kresse and J. Hafner, *Ab initio* molecular dynamics for liquid metals, Phys. Rev. B **47**, 558 (1993).

[16] G. Kresse, J. Furthmüller, and J. Hafner, Theory of the crystal structures of selenium and tellurium: The effect of generalized-gradient corrections to the local-density approximation, Phys. Rev. B **50**, 13181 (1994).

[17] G. Kresse and J. Furthmüller, Efficiency of *ab-initio* total energy calculations for metals and semiconductors using a plane-wave basis set, Comput. Mater. Sci. **6**, 15 (1996).

[18] D. Joubert, From ultrasoft pseudopotentials to the projector augmented-wave method, Phys. Rev. B **59**, 1758 (1999).

[19] J. P. Perdew, J. A. Chevary, S. H. Vosko, K. A. Jackson, M. R. Pederson, D. J. Singh, and C. Fiolhais, Erratum: Atoms, molecules, solids, and surfaces: Applications of the generalized gradient approximation for exchange and correlation, Phys. Rev. B **48**, 4978 (1993).

[20] J. Li, S. Zhang, C. Li, Y. Zhu, J. A. Boscoboinik, X. Tong, J. T. Sadowski, G. Wang, and G. Zhou, Coupling between bulk thermal defects and surface segregation dynamics, Phys. Rev. B **104**, 085408 (2021).

[21] K. Hu, M. Wu, S. Hinokuma, T. Ohto, M. Wakisaka, J. I. Fujita, and Y. Ito, Boosting electrochemical water splitting: via ternary NiMoCo hybrid nanowire arrays, J. Mater. Chem. A **7**, 2156 (2019).

[22] L. Houssiau and P. Bertrand, Direct observation of the rippling and the order-disorder transition at the Cu$_3$Au(100) surface by TOF-ion scattering, Surf. Sci. **352–354**, 978 (1996).

[23] S. Terreni, M. Canepa, L. Mattera, and V. A. Esaulov, The structure of the Cu$_3$Au(001) surface studied by impact collision of low energy Ne ions, Nucl. Instrum. Methods Phys. Res. B **193**, 550 (2002).

[24] W. E. Wallace and G. J. Ackland, Calculated energies and relaxations of the low-index planes of ordered Cu$_3$Au, Surf. Sci. **275**, L685 (1992).

[25] Z. Q. Wang, Y. S. Li, C. K. C. Lok, J. Quinn, F. Jona, and P. M. Marcus, Atomic and electronic structure of a surface alloy—comparison with the bulk alloy, Solid State Commun. **62**, 181 (1987).

[26] H. Niehus and C. Achete, Surface structure investigation of nitrogen and oxygen on Cu$_3$Au(100), Surf. Sci. **289**, 19 (1993).

[27] C. Mannori, T. Scimia, P. Cantini, S. Terreni, M. Canepa, and L. Mattera, The Cu$_3$Au(001) surface: A He diffraction study, Surf. Sci. **433–435**, 307 (1999).

[28] F. Wang, J. M. Zhang, Y. Zhang, and V. Ji, Structural properties and diffusion processes of the Cu$_3$Au(001) surface, Appl. Surf. Sci. **256**, 7083 (2010).

[29] T. Fujita, Y. Okawa, Y. Matsumoto, and K. ichi Tanaka, Phase boundaries of nanometer scale $c(2 \times 2)$-O domains on the Cu(100) surface, Phys. Rev. B **54**, 2167 (1996).

[30] H. Iddir, D. D. Fong, P. Zapol, P. H. Fuoss, L. A. Curtiss, G. W. Zhou, and J. A. Eastman, Order-disorder phase transition of the Cu(001) surface under equilibrium oxygen pressure, Phys. Rev. B **76**, 241404(R) (2007).

[31] A. A. Leitão, L. G. Dias, M. Dionízio Moreira, F. Stavale, H. Niehus, C. A. Achete, and R. B. Capaz, Signatures of oxygen on Cu$_3$Au(100): From isolated impurity to oxide regimes, Phys. Rev. B **82**, 045408 (2010).

[32] K. Oka, Y. Tsuda, T. Makino, M. Okada, M. Hashinokuchi, A. Yoshigoe, Y. Teraoka, and H. Kasai, The effects of alloying and segregation for the reactivity and diffusion of oxygen on Cu$_3$Au(111), Phys. Chem. Chem. Phys. **16**, 19702 (2014).

[33] M. Okada, Y. Tsuda, K. Oka, K. Kojima, W. A. Diño, A. Yoshigoe, and H. Kasai, Experimental and theoretical studies on oxidation of Cu-Au alloy surfaces: Effect of bulk Au concentration, Sci. Rep. **6**, 31101 (2016).

[34] W. A. Saidi, M. Lee, L. Li, G. Zhou, and A. J. H. McGaughey, *Ab initio* atomistic thermodynamics study of the early stages of Cu(100) oxidation, Phys. Rev. B **86**, 245429 (2012).

[35] M. Lee and A. J. H. McGaughey, Energetics and kinetics of the $c(2 \times 2)$ to $(2\sqrt{2} \times \sqrt{2})R45°$ transition during the early stages of Cu(100) oxidation, Phys. Rev. B **83**, 165447 (2011).

[36] A. Posada-Borbón, B. Hagman, A. Schaefer, C. Zhang, M. Shipilin, A. Hellman, J. Gustafson, and H. Grönbeck, Initial oxidation of Cu(100) studied by x-ray photo-electron spectroscopy and density functional theory calculations, Surf. Sci. **675**, 64 (2018).

[37] H. H. Brongersma, M. Carrere-Fontaine, R. Cortenraad, A. W. Denier Van Der Gon, P. J. Scanlon, I. Spolveri, B. Cortigiani, U. Bardi, E. Taglauer, S. Reiter, S. Labich, P. Bertrand, L. Houssiau, S. Speller, S. Parascandola, H. Ünlü-Lachnitt, and W. Heiland, A round robin experiment of elemental sensitivity factors in low-energy ion scattering, Nucl. Instrum. Methods Phys. Res. B **142**, 377 (1998).

[38] D. Wu, Q. Liu, J. Li, J. T. Sadowski, and G. Zhou, Visualizing reversible two-dimensional phase transitions in oxygen chemisorbed layers, J. Phys. Chem. C **122**, 28233 (2018).

[39] D. Wu, J. Li, and G. Zhou, Oxygen adsorption at heterophase boundaries of the oxygenated Cu(110), Surf. Sci. **666**, 28 (2017).

[40] W. A. Johnson and R. Mehl, Reaction kinetics in processes of nucleation and growth, Trans. Am. Inst. Min. Metall. Eng. **135**, 416 (1939).

[41] M. Fanfoni and M. Tomellini, The Johnson-Mehl-Avrami-Kolmogorov model: A brief review, Nuov. Cim. D **20**, 1171 (1998).

[42] X. Wang, J. C. Hanson, A. I. Frenkel, J. Y. Kim, and J. A. Rodriguez, Time-resolved studies for the mechanism of reduction of copper oxides with carbon monoxide: Complex behavior of lattice oxygen and the formation of suboxides, J. Phys. Chem. B **108**, 13667 (2004).

[43] A. Wilson, R. Bernard, Y. Borensztein, B. Croset, H. Cruguel, A. Vlad, A. Coati, Y. Garreau, and G. Prévot, Critical Au concentration for the stabilization of Au-Cu nanoparticles on rutile against dissociation under oxygen, J. Phys. Chem. Lett. **6**, 2050 (2015).

[44] Q. Liu, Y. Ning, W. Huang, Q. Fu, F. Yang, and X. Bao, Origin of the thickness-dependent oxidation of ultrathin Cu films on Au(111), J. Phys. Chem. C **122**, 8364 (2018).

[45] A. A. Leitão, M. D. Moreira, L. G. Dias, A. M. Silva, R. B. Capaz, and C. A. Achete, *Ab initio* studies of pristine and oxidized Cu$_3$Au(100) and (111) surfaces, J. Mater. Sci. **47**, 7594 (2012).

[46] O. Bauer, C. H. Schmitz, J. Ikonomov, M. Willenbockel, S. Soubatch, F. S. Tautz, and M. Sokolowski, Au enrichment and vertical relaxation of the Cu$_3$Au(111) surface studied by normal-incidence x-ray standing waves, Phys. Rev. B **93**, 235429 (2016).

[47] G. K. Wertheim, L. F. Mattheiss, and D. N. E. Buchanan, Partial densities of states of ordered Cu$_3$Au, Phys. Rev. B **38**, 5988 (1988).

[48] M. T. Lin, J. Shen, W. Kuch, H. Jenniches, M. Klaua, C. M. Schneider, and J. Kirschner, Growth, morphology, and crystalline structure of ultrathin Fe films on Cu$_3$Au(100), Surf. Sci. **410**, 290 (1998).

[49] G. C. S. Valadares, F. M. T. Mendes, M. Dionízio Moreira, A. A. Leitão, H. Niehus, R. B. Capaz, and C. A. Achete, Structural determination of stable MoO_x monolayers on $O/Cu_3Au(100)$: DFT calculations, Chem. Phys. **406**, 47 (2012).

[50] M. Hashinokuchi, A. Yoshigoe, Y. Teraoka, and M. Okada, Temperature dependence of Cu_2O formation on $Cu_3Au(110)$ surface with energetic O_2 molecular beams, Appl. Surf. Sci. **287**, 282 (2013).

[51] A. M. Silva, C. A. Achete, and R. B. Capaz, First-principles study of oxygen-induced copper segregation in $Cu_3Au(111)$, Chem. Phys. **410**, 99 (2013).

[52] F. U. Renner, G. A. Eckstein, L. Lymperakis, A. Dakkouri-Baldauf, M. Rohwerder, J. Neugebauer, and M. Stratmann, *In situ* scanning tunneling microscopy study of selective dissolution of Au_3Cu and $Cu_3Au(001)$, Electrochim. Acta **56**, 1694 (2011).

[53] R. F. Shannon, S. E. Nagler, C. R. Harkless, and R. M. Nicklow, Time-resolved x-ray-scattering study of ordering kinetics in bulk single-crystal Cu_3Au, Phys. Rev. B **46**, 40 (1992).

[54] Y. Huang and J. M. Cowley, A study of the $Cu_3Au(110)$ surface structure by RHEED, Surf. Sci. **285**, 42 (1993).

[55] M. Okada, M. Hashinokuchi, M. Fukuoka, T. Kasai, K. Moritani, and Y. Teraoka, Protective layer formation during oxidation of $Cu_3Au(100)$ using hyperthermal O_2 molecular beam, Appl. Phys. Lett. **89**, 201912 (2006).

[56] M. Dionízio Moreira, G. N. Fontes, H. Niehus, C. A. Achete, and R. B. Capaz, First-principles calculations and XPS

measurements of gold segregation at the $Cu_3Au(111)$ surface, J. Vac. Sci. Technol. B **30**, 051802 (2012).

[57] G. W. Zhou, J. A. Eastman, R. C. Birtcher, P. M. Baldo, J. E. Pearson, L. J. Thompson, L. Wang, and J. C. Yang, Composition effects on the early-stage oxidation kinetics of (001) Cu-Au alloys, J. Appl. Phys. **101**, 033521 (2007).

[58] L. Luo, Y. Kang, J. C. Yang, and G. Zhou, Effect of gold composition on the orientations of oxide nuclei during the early stage oxidation of Cu-Au alloys, J. Appl. Phys. **111**, 083533 (2012).

[59] L. Luo, Y. Kang, J. C. Yang, D. Su, E. A. Stach, and G. Zhou, Comparative study of the alloying effect on the initial oxidation of Cu-Au(100) and Cu-Pt(100), Appl. Phys. Lett. **104**, 121601 (2014).

[60] G. W. Zhou, L. Wang, R. C. Birtcher, P. M. Baldo, J. E. Pearson, J. C. Yang, and J. A. Eastman, Cu_2O Island Shape Transition during Cu-Au Alloy Oxidation, Phys. Rev. Lett. **96**, 226108 (2006).

[61] L. Luo, Y. Kang, Z. Liu, J. C. Yang, and G. Zhou, Effect of oxygen pressure on the initial oxidation behavior of Cu and Cu-Au alloys, MRS Online Proceedings Library **1318**, 706 (2011).

[62] R. J. Chimentão, F. Medina, J. L. G. Fierro, J. Llorca, J. E. Sueiras, Y. Cesteros, and P. Salagre, Propene epoxidation by nitrous oxide over Au-Cu/TiO_2 alloy catalysts, J. Mol. Catal. A Chem. **274**, 159 (2007).

[63] C. Della Pina, E. Falletta, and M. Rossi, Highly selective oxidation of benzyl alcohol to benzaldehyde catalyzed by bimetallic gold-copper catalyst, J. Catal. **260**, 384 (2008).